Building elastic solid electrolyte interphases for stabilizing microsized antimony anodes in potassium ion batteries

Xiaoqiong Du[+], Yao Gao[+], Biao Zhang*

X. Du, Dr. Y. Gao and Prof. B. Zhang

Department of Applied Physics, The Hong Kong Polytechnic University, Hung Hom, Hong Kong, China.

* Email: biao.ap.zhang@polyu.edu.hk

Keywords: Antimony • atomic force microscopy • energy conversion • potassium ion batteries • solid electrolyte interphase

Abstract: Alloy anodes composed of microsized particles receive increasing attention recently, which outperform the nanostructured counterparts in both the manufacturing cost and volumetric energy density. However, the pulverization of particles and fracture of solid electrolyte interphase (SEI) during cycling brings about fast capacity degradation. Herein, we show the normally considered fragile SEI could become highly elastic through electrolyte chemistry regulation. Compared to the SEI constructed in classic carbonate electrolyte, the atomic force microscopy (AFM) tests reveal that the one built in ether-based electrolyte doubles the maximum elastic strain to accommodate the repeated swelling-contracting. Such an SEI effectively encapsulates the microsized Sb anodes to prevent the capacity loss from particle isolation. Coupled with an intercalation-assisted alloying reaction mechanism, a sustained capacity of about 618 mAh g^{-1} with outstanding initial Coulombic efficiency (ICE) is obtained, which is among the highest values achieved in K-ion batteries. This work emphasizes the significance of building robust SEI, which offers the opportunity to enable stable microsized alloy anodes.

Introduction

Alloy anodes such as Si, Sn, and Sb have long been considered promising alternatives to carbon counterparts for high-energy alkali-metal ion batteries.[1] These anodes could uptake several ions per atom through alloy reactions, delivering exceptional capacities at appropriate potentials.[2] Accompanying with the alloying process, the electrode undergoes severe volume expansion, which triggers the pulverization of active particles and the breakage of solid electrolyte interphase (SEI), leading to rapid capacity degradation.[3] The SEI is formed on the anode surface in the first discharge as a result of electrolyte decomposition.[4] Successful application of modern Li-ion batteries relies largely on the ion conductive and electron insulated SEI, enabling a high Coulombic efficiency by preventing the further reduction of electrolyte in the following cycles. The massive volume expansion of alloy anodes poses a great challenge in maintaining an intact SEI. Owing to the fracture of particles, the newly exposed surface will continuously react with electrolyte once SEI is broken, which decreases the energy density due to excessive consumption of the charges from the cathodes. Meanwhile, the thick and sporadic SEI may isolate the fragmented particles from active alloy/de-alloy.[5]

Considerable amounts of works have been devoted to protecting SEI in alloy anodes through fabricating delicate nanostructures.[6] The core-shelled structure is widely prepared, where an inactive or less-expanded material during cycling is coated on the surface of alloy anodes.[7] Abundant voids are left in the core part to trigger the inward expansion, while the out layer shields the alloy from exposing the fresh surface to the electrolytes.[8] The synthesis of alloy/carbon nanocomposites is another strategy that has been extensively explored.[9]. The approach has demonstrated superiority in prolonging the cyclic life of alloy anodes but brought about other adverse effects on the battery performance. A large initial irreversible capacity is spotted due to the copious SEI formation on the high-surface-area nanomaterials. Moreover, the presence of pores/voids and large portions of carbon inevitably decreases the volumetric energy density of batteries.

Rather than passively protecting the weak SEI, most recent works have shown the benefits of reinforcing its mechanical properties. A LiF-rich SEI is constructed in Wang's group,[10] realizing stable cycling of microsized Si, Bi, and Al anodes in Li-ion batteries. Our previous works also reveal unusual stability of Sn microparticles upon sodiation/de-sodiation with the assistance of glyme electrolyte-derived SEI, which could be readily applied to Bi anodes.[11] These exciting results suggest that we could turn the problematic SEI into a treasure to help stabilize alloy anodes if well designed. The direct utilization of microparticles not only

reduces the manufacturing cost but also significantly increases the energy density of batteries. The extension of such approaches into potassium ion batteries (PIBs) is not straightforward, considering the more severe volume expansion during potassiation than that in Li- and Na- ion counterparties.[12] It has been reported that microsized Bi particles could be stabilized in glyme-based electrolytes due to the construction of robust SEI and the formation of a unique porous structure that partly relieves the stress.[13] However, the same strategy fails to work in neat Sb anodes which present much higher theoretical capacity than Bi. The reason is likely ascribed to the absence of pore formation during cycling, thus requiring optimization of both electrode composition and binder as well as utilization of high-concentration electrolytes.[14] Moreover, a detailed relationship between the mechanical properties and electrochemical stability remains unclear. Herein, we demonstrate the Sb microparticles with unprecedented performance could be realized through electrolyte chemistry regulation. A robust SEI is built with the assistance of 1 M KFSI/ethylene glycol diethyl ether (EGDE) electrolyte, enabling a high reversible capacity of 618 mAh g^{-1} at 0.1 A g^{-1} with outstanding cyclic and rate performance. To explore the underlying mechanism for the unusual stability, atomic force microscopy (AFM) is adopted to characterize the mechanical properties of the SEI. It reveals the highly elastic nature of the SEI formed in EGDE-derived electrolyte, which is beneficial to accommodating the volume change of the electrode. This works offers an alternative SEI-derived approach to design advanced Sb anodes for PIBs.

Results and Discussion

Commercial Sb with an average particle size of 5.9 μm is used as active materials (**Figure S1a and b**). The powder is mixed with conductive carbon and carboxymethylcellulose sodium (CMC) binder by low-energy planetary ball milling for four hours to make the electrode. X-ray powder diffraction (XRD) patterns show that the (003) and (006) planes of Sb become negligible after ball milling compared with the untreated ones (**Figure S1e**). The shear force during mechanical ball milling partly exfoliates the Sb along the c-axis and reduces its thickness, which has also been observed in previous studies.[15] Consequently, the average particle size of Sb is reduced to approximately 1.1 μm (**Figure S1c and d**). Nevertheless, the crystallinity of Sb is well preserved, as indicated by the prominent (012), (104), and (110) peaks. We first evaluate the electrochemical performance in classic carbonate electrolytes (ECPC) with the potassium bis(fluorosulfony)imide (KFSI) as the salt, which has been reported beneficial in SEI formation.[16] In **Figure 1a**, the cell shows a reversible capacity of

517.8 mAh g^{-1} in the first cycle with a low initial Coulombic efficiency (ICE) of 56.5% due to the severe electrolyte decomposition.

In contrast, the Sb electrode cycled in ethylene glycol diethyl ether (EGDE) based electrolyte presents a capacity of 800.8 and 555.7 mAh g^{-1} in the first discharge and charge, respectively, corresponding to a remarkable ICE of 69.4% (**Figure 1b**). The electrolyte formulation plays a critical role in determining the ICE, where EGDE solvent outperforms the ECPC counterpart. It implies a stable SEI is formed in EGDE-based electrolyte, effectively preventing the exposure of new Sb surface as will be discussed later. The long-term cyclic stability is examined under 0.1 A g^{-1} (**Figure 1c**). The capacity slightly increases due to the gradual activation of the bulk material.[17] A reversible capacity of 573 mAh g^{-1} is obtained in EGDE-based electrolyte after the 180th cycle, corresponding to the insertion of 2.60 K ions per Sb atom, which is close to the value predicted by theoretical calculation.[12] To our best knowledge, the value reported here is the highest for the microsized anodes in PIBs. The capacity retention of nearly 100% (compared to the first reversible capacity) is achieved after 180 cycles, whereas the cell cycled in ECPC-based electrolyte completely loses the activity in 60 cycles. We also evaluate the long-term cyclic performance at a high current density of 0.5 A g^{-1}, showing a capacity of 443 mAh g^{-1} after 150 cycles. The performance could be further improved by either limiting the cut-off voltage to 0-1.0 V or through synthesis of Sb particles with reduced particle size (~500 nm) (**Figure S2**). The reversible capacity and superior ICE obtained in EGDE-based electrolyte offer a very competitive performance among the Sb-based electrodes for PIBs, without resorting to nanostructure design and high concentration electrolyte (**Table S1**). Note that the stable cyclic performance cannot be achieved in the classic ether-based electrolytes, such as 1 M KFSI/DME and 1 M KFSI/DGME (**Figure S3**). For sake of completeness, we evaluate the Sb performance for Li and Na ion storage under EGDE-derived electrolyte, which also shows improved cyclic stability (**Figure S4**).

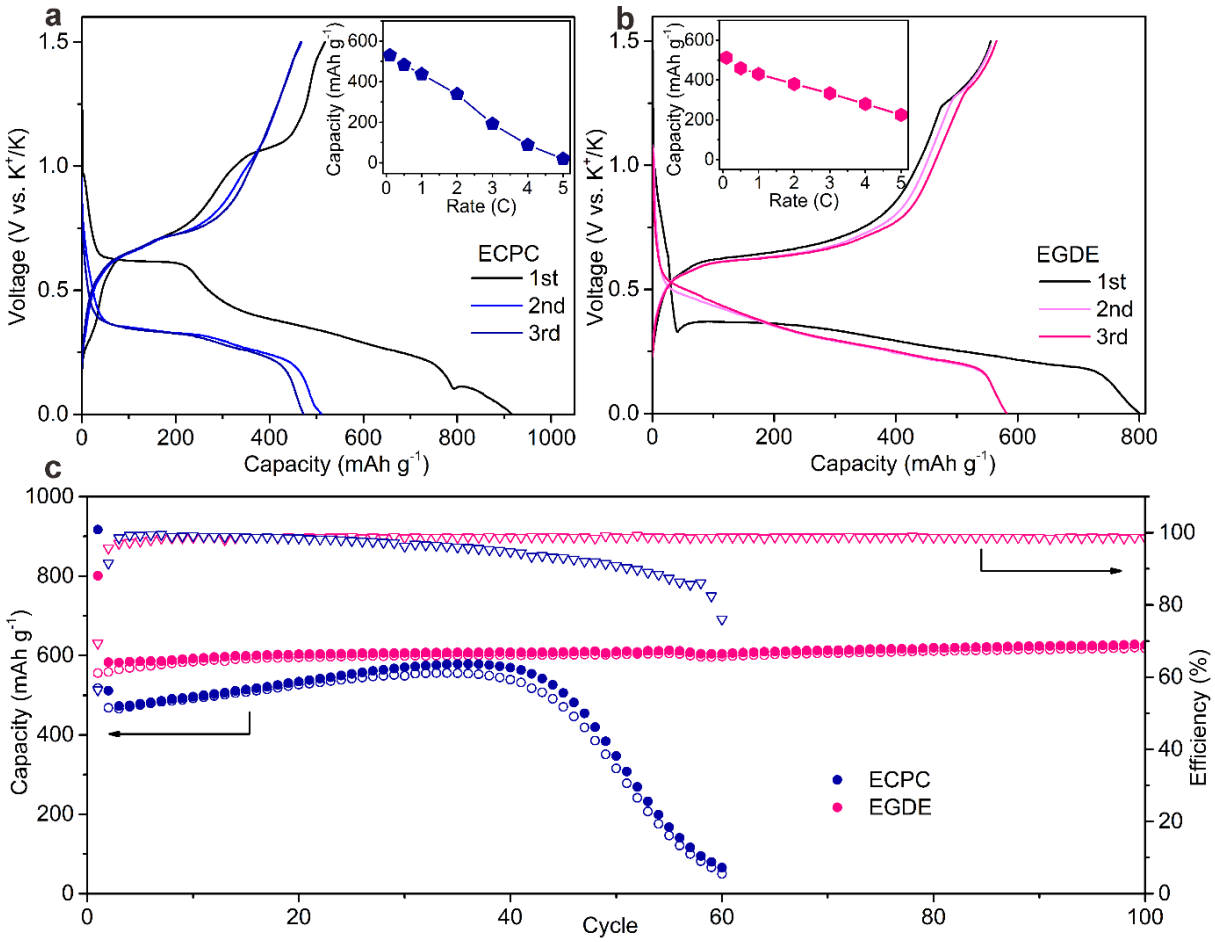

Figure 1. Electrochemical performance of Sb electrodes. The galvanostatic discharge-charge profiles in (a) 1 M KFSI/ECPC and (b) 1 M KFSI/EGDE electrolytes of selected cycles under 0.1 A g^{-1} (inset: rate performances). (c) Cyclic performance under 0.1 A g^{-1}.

Apart from the stability, the voltage profiles of EGDE-based electrolyte show a much lower polarization, suggesting faster kinetics. Therefore, we evaluate the rate capability of cells in the two electrolytes and explore the charge transfer at the interface. In EGDE-based electrolyte, the Sb electrode delivers decent performance at increasing current densities, i.e., 430 and 225 mAh g^{-1}at 1C and 5C (1C=660 mA g^{-1}), respectively (**Figure 1b inset and Figure S5**). In contrast to this, the electrode shows negligible capacity in ECPC-based electrolyte when the current density increases to 5C (**Figure 1a inset and Figure S5**). The reason lies in the slow kinetics at the electrode/electrolyte interface, as demonstrated in electrochemical impedance spectroscopy (EIS) spectra of the electrodes at OCV and after three cycles. The fitted data using an equivalent circuit (**Figure S6 and Table S2**) shows that both the charge transfer (R_{ct}) and SEI resistance (R_{SEI}) in EGDE-based electrolyte is much smaller than those in ECPC-based electrolyte. The galvanostatic intermittent titration technique (GITT) is conducted

for comparing the diffusion coefficient in ECPC and EGDE electrolytes, which does not show big different due to the similar phase transformation process (**Figure S7**).

The CV curve (**Figure S8**) presents three peaks located at around 0.48, 0.21 and 0.14 V upon potassiation, indicating a multiple-step phase transformation. The K-Sb phase diagram has been extensively studied by computational approaches,[14b, 18] but the experimental results suggest a distinct reaction path. A final agreement is yet to be achieved due to the complexity of the electrochemical processes. The phase transformation during K-Sb alloy/de-alloy is systematically studied by in situ XRD (**Figure 2a, Figure S9**). The XRD pattern at open circuit voltage (OCV) state shows three pronounced peaks at 28.5 º, 39.8 º, and 41.7 º corresponding to (012), (104), and (110) facets of Sb (PDF#35-0732), respectively. The intensities of these peaks gradually decrease during discharge. A new phase emerges at around 0.4 V with three characteristic peaks at 19.5 º, 22.6 º, and 32.3 º. By excluding SEI formation related capacity, the discharge capacity indicates approximately 0.5 K ions have been alloyed with per Sb atom at this potential. It agrees well with the theoretical prediction where $K_{0.5}Sb$ would be the first alloy phase in K-Sb phase diagram,[19] but the detailed crystal structure could not be resolved here due to the poor crystallinity. The next phase appears when discharges to 0.25 V, which could be indexed as K_1Sb having a layered structure that belongs P4/mmm space group. K_1Sb phase consists of an Sb layer with intercalated K in-between (**Figure S10**), deriving from Li_1Sb structure.[20] Surprisingly, further discharge does not lead to the formation of any new phase before reaching nearly 0 V, although density functional theory (DFT) calculation suggests the existence of K_5Sb_4.[18] The major observation between 0.25 V and 0 V is the leftward shift of the peaks related to the K_1Sb phase. It reflects the broadening of the interlayer distance arising from the intercalation of K ions into the lamellar K_1Sb to form $K_{1+x}Sb$. This phenomenon is unusual in the alloy-type anodes, where staging-like behaviour normally takes place due to the phase transformation between intermediate alloy phases.[21] The cubic K_3Sb phase appears at the end of discharge (0 V). The minor amount of K_1Sb and $K_{0.5}Sb$ remains due possibly to the incomplete reaction stemming from the imperfect contact of the in situ cell. To avoid any artefact, we also conduct the ex situ XRD to allow a full reaction (**Figure S11**). All the intermediate phases are transferred to K_3Sb in the electrode ex situ discharged to 0 V; beside the cubic K_3Sb phase that captured in the in situ test, hexagonal K_3Sb is also detected. Part of the cubic K_3Sb phase is transferred into the hexagonal one, suggesting the latter is more thermodynamically stable. [22]

Upon charging, the potassiated K_3Sb phase returns to Sb following the reversed reaction path. A de-intercalation from $K_{1+x}Sb$ is observed as reflected by the rightward shift of the XRD

peak starting from 0.37 V. It confirms the presence of intercalation/de-intercalation behaviour in K_1Sb phase, owing to the layered structure nature. A similar phenomenon has been reported in antimonene upon Li/Na insertion but has not been clearly spotted in K-Sb system.[23] Compared to the alloying process, the intercalation induces less structural deterioration to the electrodes.[24] The presence of the intercalation process enables the gradual volume change to prevent the structural collapse from sudden expansion. Once charging to 1.5 V, the Sb phase reappears although with reduced crystallinity, evidencing the reversibility of K-Sb alloy/de-alloy reactions (**Figure S11**). The phase transformation process is summarized in **Figure 2b**. An intercalation phase K_1Sb presents before reaching the end cubic K_3Sb alloy. The latter could be partly transmitted into hexagonal allotropy as indicated by the dashed line. Noteworthy that neither the ball milling nor electrolyte affects the phase transformation (**Figure S12**).

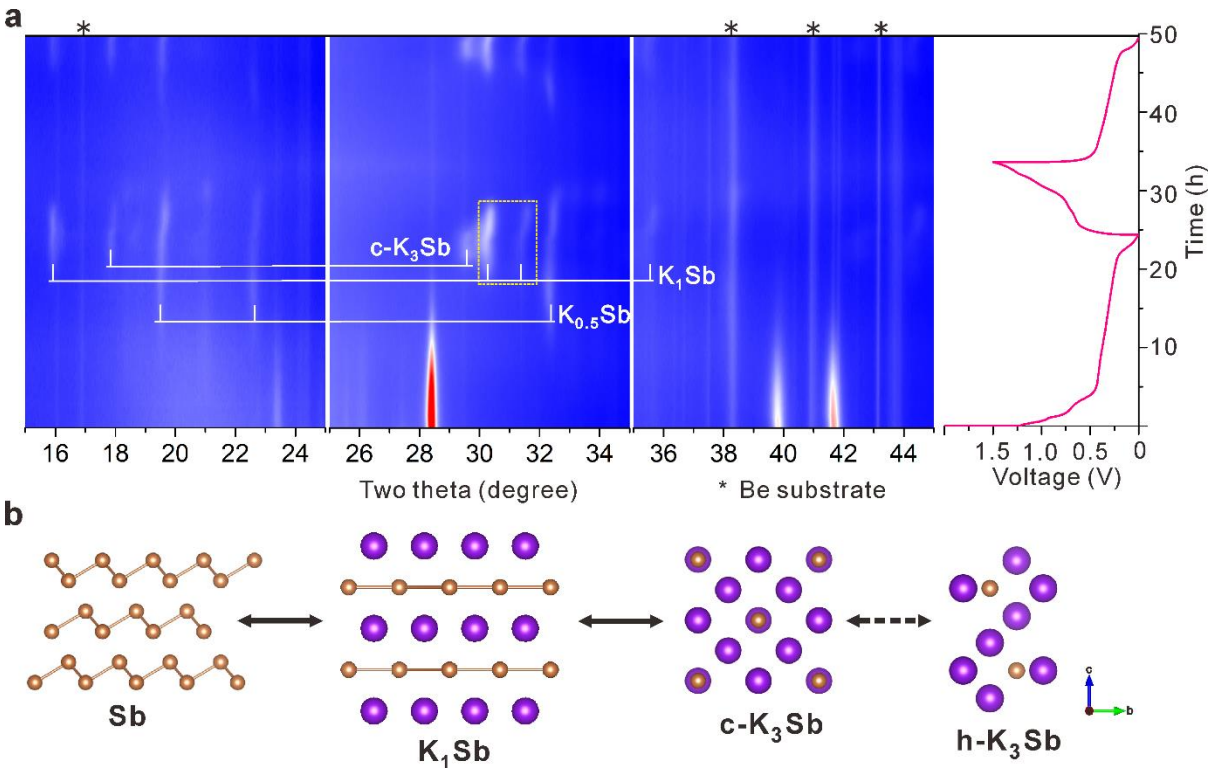

Figure 2. (a) Contour map of in situ XRD for ball-milled Sb electrode in 1 M KFSI/EGDE electrolyte on the first two cycles under 0.05 A g^{-1} (peak-shift is marked in rectangle frame). (b) Schematic of the phase transformations, where c-K_3Sb and h-K_3Sb represent cubic and hexagonal K_3Sb, respectively (Dash arrow stands for coexistence). Detailed lattice parameters of these phases are listed in **Table S3**.

A large relative volume expansion of 407% is induced when the Sb is transformed into K_3Sb,[22] which may cause the fracture of both active particles and SEI. The integrity of Sb electrodes cycled in EGDE and ECPC-based electrolytes are investigated by transmission

electron microscopy (TEM) and scanning transmission electron microscopy (STEM). Apparent cracks in the Sb microparticles are observed after cycling in ECPC-based electrolytes (**Figure 3a**). Meanwhile, numerous tiny particles present on the edge of the pristine material (**Figure 3b and c**), which can be indexed as (110) lattice of cubic Sb (ICSD#9013008) with d-spacing of 2.2 Å and 90 º intersection angle. It can be inferred that those small cubic Sb particles are originated from the pulverization of Sb host. Surprisingly, there is no clear boundary between the SEI layer and the active material. SEI is expected to form in the first discharge as a result of electrolyte decomposition. Ideally, the SEI would encapsulate the particles and isolate them from the electrolyte. We speculate that the SEI breaks in traditional carbonate electrolytes during the K-Sb alloy process owing to the enormous volume expansion. Consequently, the newly exposed surface from the fragmented particles contacts again with the electrolyte, leading to the re-decomposition of the electrolyte to form additional SEI, which wrapped the tiny particles. The repeated particle fracture and SEI reconstruction result in a super thick SEI with tiny Sb enclosed. As demonstrated in STEM image (**Figure S13**), the thickness of SEI could reach around 50 nm with variation in localized positions. Such a process, as illustrated in **Scheme 1**, brings about electrode deterioration in several aspects. Firstly, the SEI fracture-formation continuously consume the K ions, giving rise to low Coulombic efficiency. Meanwhile, the resulted thick SEI layer increases the charge transfer resistance, as shown in EIS measurement, which severely decreases the rate capability. Furthermore, the fragmented particles may completely lose the electrical contact to become inactive for K ions uptake, resulting in the capacity degradation that has been observed in the cyclic test.

Compared to the electrode cycled in ECPC-based electrolyte, the one prepared in EGDE counterpart possesses an intact morphology after three cycles (**Figure 3d**). Although small cracks arising from internal stress is discerned, the integrity of microsized particles is well preserved. The enlarged image (**Figure 3e**) shows a sharp discrepancy, where none of the fragmented particles are detected. A thinner SEI with a thickness of around 20 nm is covered on the Sb. The SEI formed here has an almost amorphous structure. Only minor amounts of crystals with an extremely small size of about 3 nm is detected (**Figure 3f**). They could be indexed as the (220) lattice of K_2O (PDF#47-1701) based on the d-spacing of 2.3 Å, which is a common component of SEI in K-ion batteries.[25] The morphologies of the electrodes after long-term cycling are further investigated in ECPC (**Figure 3g-h**) and EGDE-based electrolyte (**Figure 3i-j**). Severe cracks and broken particles are found in the centre and edges of the electrode cycled ECPC based electrolyte, while the integrity of Sb particles is largely maintained after cycling in EGDE counterpart. Only slight structural change occurs on the edge

due to the repeated alloy/de-alloy, where many flakes present but without separating from the host particle. Electron energy loss (EEL) spectra analysis is conducted to deduce the components in SEI (**Figure 3k**). Obvious π*(C=O) vibration is detected in both C and O K-edge spectra for the SEI formed in ECPC-based electrolyte, due possibly to the presence of carbonate species as will be further discussed by XPS. Electron energy loss spectroscopy (EELS) elemental maps in **Figure S14 and Figure S15** clearly show the distribution of Sb, C, O, and K, where the last three elements are mainly from SEI. The observations indicate that the SEI built in EGDE-based electrolyte is able to accommodate the tremendous volume expansion, which not only constrains the particles from pulverization but also prevents the repeated SEI formation, as illustrated in **Scheme 1**. The overall morphologies of the electrodes further substantiate the above conjecture. Scanning electron microscope (SEM) images (**Figure 3l and m**) show that the microsize nature of the particles is remained in EGDE-based electrolyte, whereas particles are fragmented for those tested in ECPC equivalent. Moreover, the particles are covered by a thick SEI layer due to the continuous formation of SEI in the latter electrolyte.

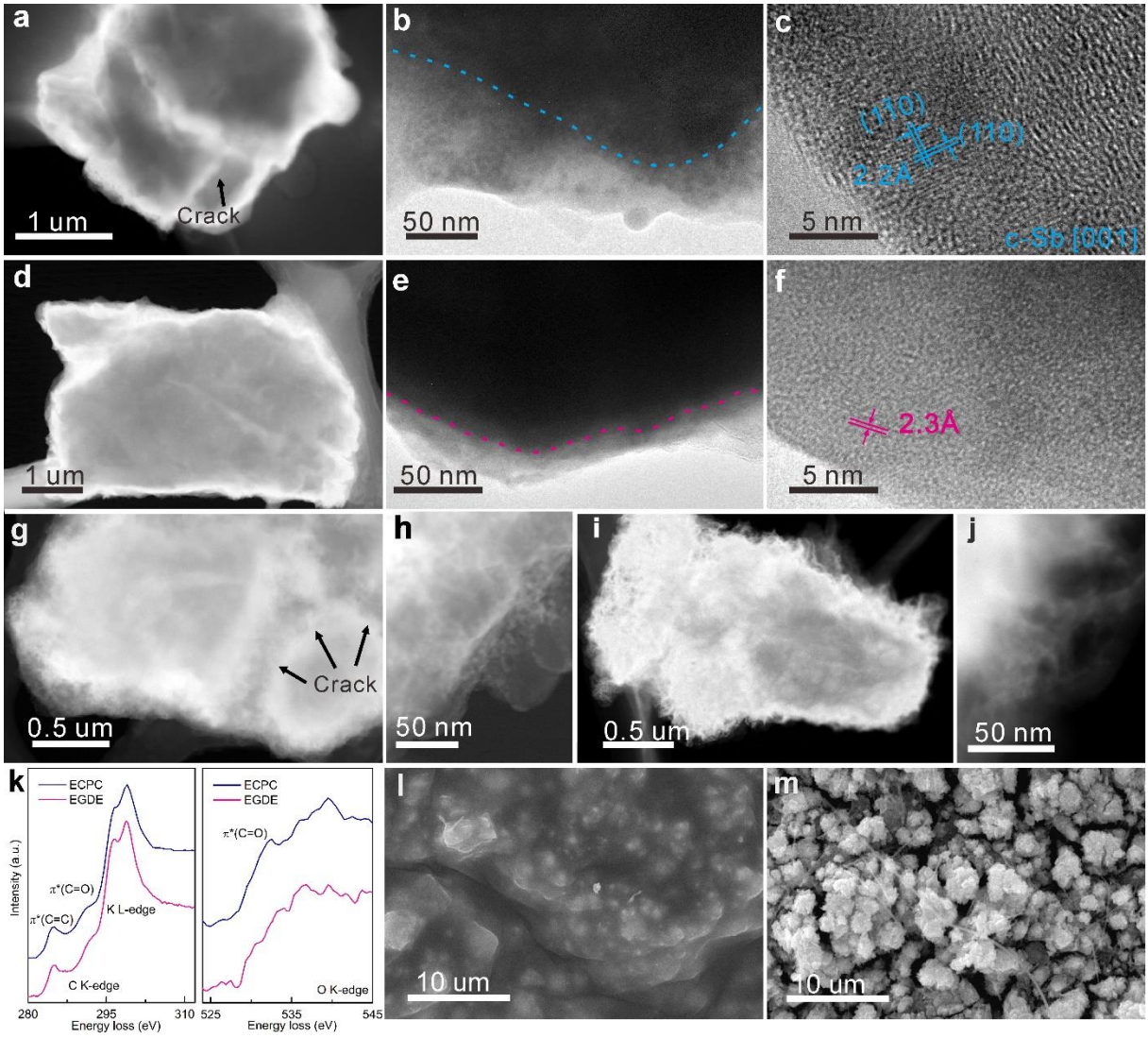

Figure 3. Morphologies and EEL spectra of cycled Sb electrodes: STEM/TEM images after 3 cycles in (a-c) 1 M KFSI/ECPC and (d-f) 1 M KFSI/EGDE; after 50 cycles in (g-h) 1 M KFSI/ECPC and (i-j) 1 M KFSI/EGDE. (k) EEL spectra after 50 cycles. SEM images after 100 cycles in (l) 1 M KFSI/EGDE, and (m) 1 M KFSI/ECPC.

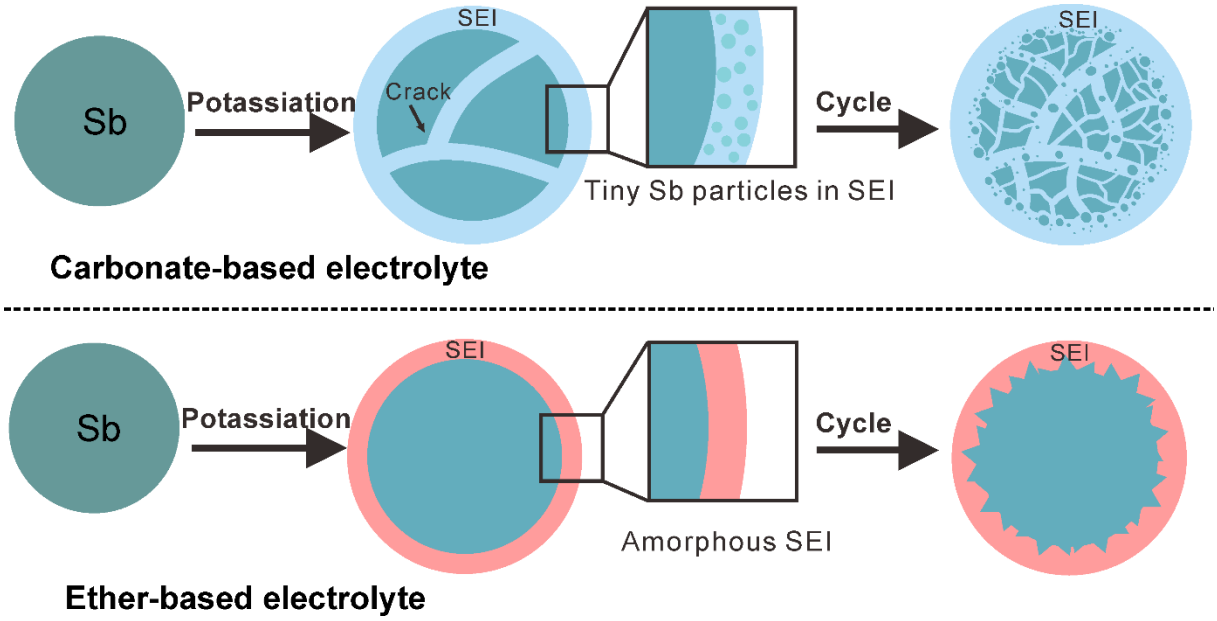

Scheme 1 Illustration of electrode/SEI evolution in ECPC (up) and EGDE-based (down) electrolytes.

The capability of SEI in buffering the volume expansion comes as a surprise, as it is considered the most fragile part, which requires prudent protection in previous reports.[26] Therefore, we evaluate the mechanical properties of SEI by the atomic force microscopy (AFM) technique in the Ar filled glovebox. To exclude the interference from binder and carbon additives, a neat Sb film is coated on Cu foil through electrodeposition. The Sb has the same crystal structure as the one used in the conventional electrode (**Figure S16**). The electrode is charged/discharged for three cycles to build the SEI layer on the particles (**Figure S17**). Typical force-displacement curves obtained from the AFM-based nanoindentation tests of SEI are shown in **Figure 4a**. At point a, the AFM probe starts to contact the SEI surface with zero external force. As the AFM probe continues to move downward, the SEI begins to deform elastically. With increasing force, the SEI reaches the limit of elastic deformation, corresponding to the first discontinuity point on the force-displacement curve (point a'). We can obtain the value of Young's modulus (E) of the SEI based on the Hertz contact model.[27],[11c] Adopting the von Mises' shear strain-energy criterion or the Tresca's maximum shear stress criterion, the maximum elastic strain (ε_Y) of SEI can be obtained (Equation (S1) and (S2)).[28] **Figure 4b and c** show the AFM topography images of the electrodeposited Sb electrodes cycled in ECPC and EGDE-based electrolytes, respectively. The surface roughness factor Ra (the arithmetic mean deviation of the assessed profile) of the electrode surface is generated from topography images. After three cycles in ECPC-based electrolyte, Ra can be

calculated as 25.74 ± 4.46 nm, while the value is 70.15 ± 14.41 nm in EGDE counterpart. Besides the surface roughness, another noticeable appearance is the cracks. We statistically count the fracture pattern density (the total fracture length/area) of the two electrodes and find that the value of the electrode cycled in ECPC-based electrolyte is almost 3.63 times higher than the electrode tested in EGDE equivalent.

Figure 4d summarizes the obtained E and ε_Y values of the SEI formed in these two types of electrolytes. Compared to the SEI formed in ECPC-based electrolyte (E: 1134.97 ± 624.16 MPa, ε_Y: 0.44 ± 0.14), the one in EGDE has a smaller E value (578.05 ± 339.87 MPa) but a larger ε_Y (0.92 ± 0.42) (**Figure 4e**). The value of ε_Y determines the upper limit of the reversible deformation that the SEI can bear. Large ε_Y will be highly advantageous for the electrode with a large volume change. The ECPC-derived SEI has a high Young's modulus and poor deformation capability, which may originate from the various hard Sb (E: 55 GPa) particles encapsulated in the SEI layer, as observed in the TEM images (**Figure 3b and Figure S13**). The topographic features discussed above are in good accordance with the measured mechanical properties of SEI. The smaller Young's modulus of the SEI formed in EGDE-based electrolyte makes it less resistant to local deformation, which leads to an increase in surface roughness. The larger ε_Y makes it less likely to yield or fracture during the drastic volume change of the electrode, and results in a much lower fracture density compared to the case in ECPC. The results attest to the significance of large ε_Y of SEI in maintaining the solidity of an electrode during expansion and contraction.

The chemical composition of SEI formed in the two electrolytes is examined by X-ray photoelectron spectroscopy (XPS) to explore the origin of such a stark difference in the mechanical properties. **Figure 4f and g** show C-C/C-H, C-O, C=O, and K-F bonds in deconvoluted C1s and F1s spectra, illustrating both organic and inorganic components are involved in SEIs. The C-C/C-H bonds (284.9 eV) are mainly from the hydrocarbyl group in ECPC or EGDE-derived SEIs.[29] The alkyl carbonates species ($ROCO_2K$) are found in ECPC-developed SEI, signifying by the peak at 288.3 eV in C1s spectrum (**Figure 4g**),[30] which is consistent with EEL spectra result (**Figure 3k**). An additional C-O type bond at 286.7 eV in C1s is detected in EGDE-derived SEI, which can be assigned to polymer-like species of $[CH_2CH_2O]n$.[31] Apart from the C-O bond, the C=O bond at 289.0 eV corresponds to ethyl formate, stemming from the isomerization of EGDE with radical species.[32] These oligomers are characteristic of their high elasticity for increasing the maximum yield strain of the resulted SEI.[33] Other inorganic components that originated from the decomposition of KFSI salt such

as KF are also observed (F1s spectra in **Figure 4f and g**).[34] Compared to the SEI formed in ECPC-based electrolyte, The one in EGDE counterpart has overwhelming rich fluorine content (6.67 at.% vs. 0.72 at.%). which has been proven beneficial to improving the chemical stability of SEIs and charge transfer due to the large ratio of ionic-to-electronic conductivity.[35]

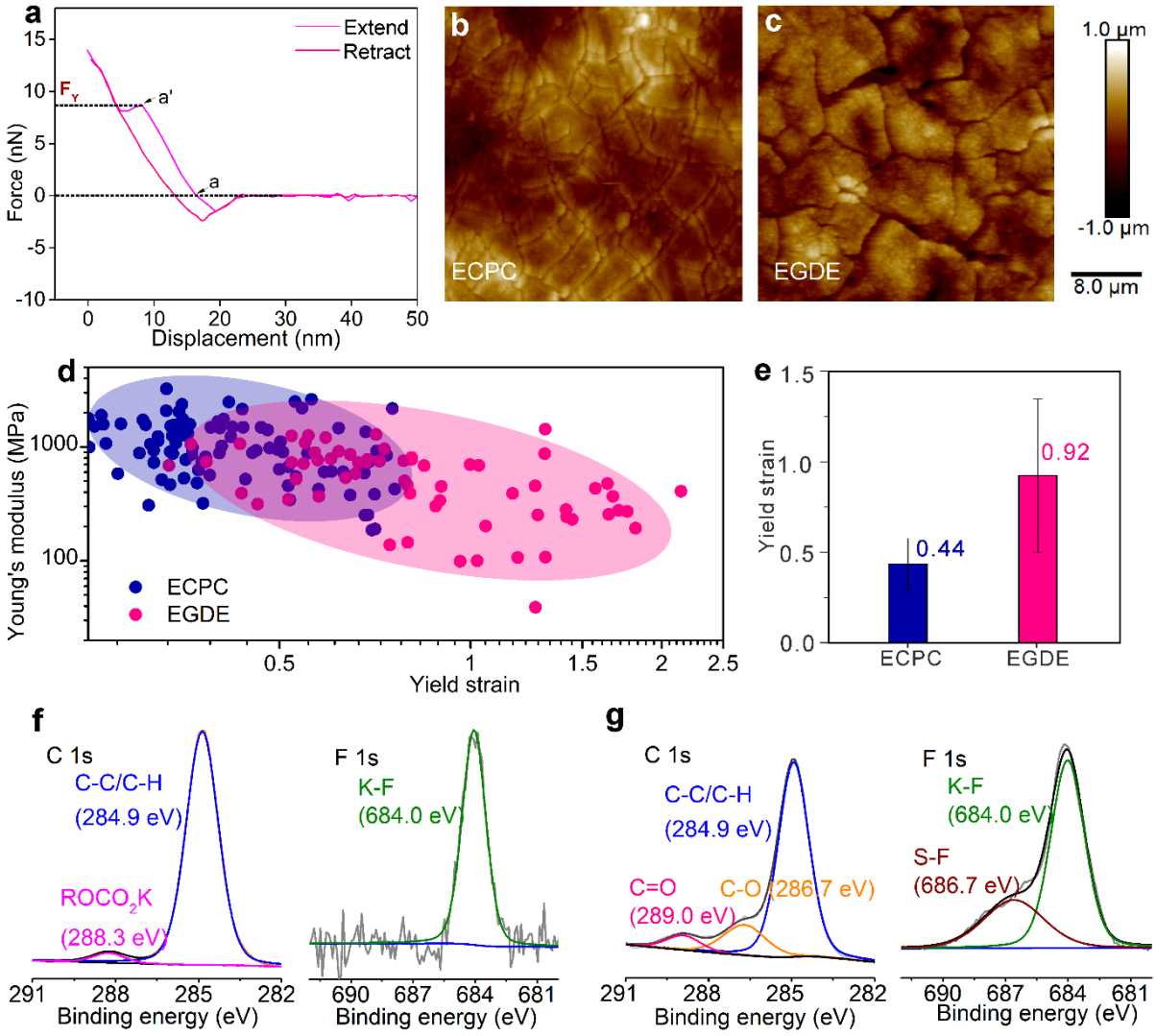

Figure 4 AFM and XPS characterizations. (a) Characteristic force curves obtained from the AFM tests on electrodeposited Sb electrodes. AFM topography images in (b) 1 M KFSI/ECPC and (c) 1 M KFSI/EGDE. (d) Distributions of Young's modulus and yield strain of SEIs. (e) Histogram with an error bar of yield strain. XPS spectra of Sb electrodes after cycling 3 times in (f) 1 M KFSI/ECPC and (g) 1 M KFSI/EGDE electrolytes.

One concern regarding the adoption of ether-based electrolytes is the poor stability against oxidation at a high voltage, which may bring difficulties in full cell assembly. To assess the full cell performance in 1 M KFSI/EGDE electrolyte, we synthesize $K_xMnFe(CN)_6$ cathode,

which has been considered promising in K-ion batteries due to the advantages in the cost.[36] The XRD confirms the standard pattern of $KMnFe(CN)_6$ (PDF#96-152-1297) (**Figure S18**). The synthesized $K_xMnFe(CN)_6$ shows an initial charge capacity of about 130 mAh g^{-1}. Therefore, the cathode to anode mass ratio of 6: 1 is adopted (**Figure S19a**). The full cell delivers a capacity of 69.4 and 53.4 mAh g^{-1} with an average potential of 2.8 V under 10 and 30 mA g^{-1} (based on the total mass of cathode and anode) (**Figure S19b-c**). The capacity could be increased to 87.5 mAh g^{-1} through eliminating SEI-induced capacity loss by pre-cycling Sb. The full cells show decent cyclic performances with an attractive energy density of about 194 and 256 Wh kg^{-1} of without and with Sb pre-cycling, respectively (**Figure S19d**).

Conclusions

The phase transformation and morphology evolution of microsized Sb anodes during K ions insertion/extraction are thoroughly investigated to resolve the poor cyclic stability. The unique intercalation-assisted alloying reaction pathway partly prevents the structural collapse from rapid volume expansion. Combining with electrolyte regulation, we achieve an outstanding capacity of 618 mAh g^{-1} for Sb microparticles, which is well maintained in the long-term cycles. We demonstrate that such stability originates from the construction of elastic SEI, which effectively encapsulates the particles during electrode expansion and contraction. The XPS analysis suggests the presence of oligomer-like species mainly accounts for the improved maximum elastic strain (ε_Y) in the EGDE-derived SEI. Compared to Young's modulus, the ε_Y plays more essential role in determining the electrode stability, which was rarely measured and discussed before when evaluating SEI's mechanical properties. These findings elaborate the structural insights to design elastic SEIs for stabilizing microsized alloy anodes, so as to boost the energy densities of today's alkali-metal ion batteries.

Acknowledgments

This work was supported by the General Research Fund (GRF) scheme of the Hong Kong Research Grants Council (Project No. 15305219), and the Hong Kong Polytechnic University (ZVRP, 1-ZE30).

Reference

[1] a) H. Wu, Y. Cui, *Nano Today* **2012**, *7*, 414-429; b) G. Derrien, J. Hassoun, S. Panero, B. Scrosati, *Adv. Mater.* **2007**, *19*, 2336-2340; c) J. Qian, Y. Chen, L. Wu, Y. Cao, X. Ai, H. Yang, *Chem. Commun.* **2012**, *48*, 7070-7072.

[2] C.-M. Park, J.-H. Kim, H. Kim, H.-J. Sohn, *Chem. Soc. Rev.* **2010**, *39*, 3115-3141.

[3] E. Peled, *J. Electrochem. Soc.* **1979**, *126*, 2047.

[4] M. B. Pinson, M. Z. Bazant, *J. Electrochem. Soc.* **2012**, *160*, A243.
[5] M. Winter, *Z. Phys. Chem.* **2009**, *223*, 1395-1406.
[6] a) P. Ge, S. Li, L. Xu, K. Zou, X. Gao, X. Cao, G. Zou, H. Hou, X. Ji, *Adv. Energy Mater.* **2019**, *9*, 1803035; b) C. Cui, J. Xu, Y. Zhang, Z. Wei, M. Mao, X. Lian, S. Wang, C. Yang, X. Fan, J. Ma, *Nano Lett.* **2018**, *19*, 538-544; c) F. Xie, L. Zhang, B. Chen, D. Chao, Q. Gu, B. Johannessen, M. Jaroniec, S.-Z. Qiao, *Matter* **2019**, *1*, 1681-1693; d) J. Wang, L. Fan, Z. Liu, S. Chen, Q. Zhang, L. Wang, H. Yang, X. Yu, B. Lu, *ACS Nano* **2019**, *13*, 3703-3713; e) X. Bian, Y. Dong, D. Zhao, X. Ma, M. Qiu, J. Xu, L. Jiao, F. Cheng, N. Zhang, *ACS Appl. Mater. Interfaces* **2019**, *12*, 3554-3562; f) J. Zhou, J. Chen, M. Chen, J. Wang, X. Liu, B. Wei, Z. Wang, J. Li, L. Gu, Q. Zhang, *Adv. Mater.* **2019**, *31*, 1807874; g) X. Zhao, J. Wang, R. Yu, D. Wang, *J. Am. Chem. Soc.* **2018**, *140*, 17114-17119.
[7] a) H. Wu, G. Chan, J. W. Choi, I. Ryu, Y. Yao, M. T. McDowell, S. W. Lee, A. Jackson, Y. Yang, L. Hu, Y. Cui, *Nat. Nanotechnol.* **2012**, *7*, 310-315; b) F. Yang, H. Gao, J. Hao, S. Zhang, P. Li, Y. Liu, J. Chen, Z. Guo, *Adv. Funct. Mater.* **2019**, *29*, 1808291; c) Y. Wu, S. Hu, R. Xu, J. Wang, Z. Peng, Q. Zhang, Y. Yu, *Nano Lett.* **2019**, *19*, 1351-1358; d) Y. Huang, Y. Fang, X. F. Lu, D. Luan, X. W. Lou, *Angew. Chem. Int. Ed. Engl.* **2020**, *132*, 20086-20090; e) Z. Li, Y. Fang, J. Zhang, X. W. Lou, *Adv. Mater.* **2018**, *30*, 1800525; f) K. Yang, J. Tang, Y. Liu, M. Kong, B. Zhou, Y. Shang, W.-H. Zhang, *ACS Nano* **2020**, *14*, 5728-5737.
[8] a) Y. An, Y. Tian, L. Ci, S. Xiong, J. Feng, Y. Qian, *ACS Nano* **2018**, *12*, 12932-12940; b) H. Yang, L.-W. Chen, F. He, J. Zhang, Y. Feng, L. Zhao, B. Wang, L. He, Q. Zhang, Y. Yu, *Nano Lett.* **2019**, *20*, 758-767.
[9] a) D. Adekoya, H. Chen, H. Y. Hoh, T. Gould, M.-S. J. T. Balogun, C. Lai, H. Zhao, S. Zhang, *ACS Nano* **2020**, *14*, 5027-5035; b) P. Xiong, J. Wu, M. Zhou, Y. Xu, *ACS Nano* **2019**, *14*, 1018-1026; c) X. Ge, S. Liu, M. Qiao, Y. Du, Y. Li, J. Bao, X. Zhou, *Angew. Chem. Int. Ed. Engl.* **2019**, *131*, 14720-14725; d) Y. Zhang, G. Wang, L. Wang, L. Tang, M. Zhu, C. Wu, S.-X. Dou, M. Wu, *Nano Lett.* **2019**, *19*, 2575-2582; e) J. Liu, L. Yu, C. Wu, Y. Wen, K. Yin, F.-K. Chiang, R. Hu, J. Liu, L. Sun, L. Gu, *Nano Lett.* **2017**, *17*, 2034-2042; f) Y. Fang, X. Y. Yu, X. W. Lou, *Angew. Chem. Int. Ed. Engl.* **2018**, *130*, 10007-10011.
[10] J. Chen, X. Fan, Q. Li, H. Yang, M. R. Khoshi, Y. Xu, S. Hwang, L. Chen, X. Ji, C. Yang, Huixin He, Chongmin Wang, Eric Garfunkel, Dong Su, Oleg Borodin, C. Wang, *Nat. Energy* **2020**, *5*, 386-397.
[11] a) B. Zhang, G. Rousse, D. Foix, R. Dugas, D. A. Corte, J. M. Tarascon, *Adv. Mater.* **2016**, *28*, 9824-9830; b) J. Huang, X. Lin, H. Tan, B. Zhang, *Adv. Energy Mater.* **2018**, *8*, 1703496; c) J. Huang, X. Guo, X. Du, X. Lin, J.-Q. Huang, H. Tan, Y. Zhu, B. Zhang, *Energy Environ. Sci.* **2019**, *12*, 1550-1557.
[12] H. Kim, J. C. Kim, M. Bianchini, D. H. Seo, J. Rodriguez‐Garcia, G. Ceder, *Adv. Energy Mater.* **2018**, *8*, 1702384.
[13] K. Lei, C. Wang, L. Liu, Y. Luo, C. Mu, F. Li, J. Chen, *Angew. Chem. Int. Ed. Engl.* **2018**, *130*, 4777-4781.
[14] a) J. Wu, Q. Zhang, S. Liu, J. Long, Z. Wu, W. Zhang, W. K. Pang, V. Sencadas, R. Song, W. Song, *Nano Energy* **2020**, *77*, 105118; b) J. Zheng, Y. Yang, X. Fan, G. Ji, X. Ji, H. Wang, S. Hou, M. R. Zachariah, C. Wang, *Energy Environ. Sci.* **2019**, *12*, 615-623; c) X. Ge, S. Liu, M. Qiao, Y. Du, Y. Li, J. Bao, X. Zhou, *Angew. Chem. Int. Ed. Engl.* **2019**, *58*, 14578-14583; d) L. Zhou, Z. Cao, W. Wahyudi, J. Zhang, J.-Y. Hwang, Y. Cheng, L. Wang, L. Cavallo, T. Anthopoulos, Y.-K. Sun, *ACS Energy Letters* **2020**, *5*, 766-776; e) Y. Tian, Y. An, S. Xiong, J. Feng, Y. Qian, *J. Mater. Chem. A* **2019**, *7*,

9716-9725; f) L. Zhou, Z. Cao, J. Zhang, H. Cheng, G. Liu, G. T. Park, L. Cavallo, L. Wang, H. N. Alshareef, Y. K. Sun, *Adv. Mater.* **2021**, 2005993.
[15] X. Wang, J. He, B. Zhou, Y. Zhang, J. Wu, R. Hu, L. Liu, J. Song, J. Qu, *Angew. Chem. Int. Ed. Engl.* **2018**, *130*, 8804-8809.
[16] a) N. Xiao, W. D. McCulloch, Y. Wu, *J. Am. Chem. Soc.* **2017**, *139*, 9475-9478; b) Q. Zhang, J. Mao, W. K. Pang, T. Zheng, V. Sencadas, Y. Chen, Y. Liu, Z. Guo, *Adv. Energy Mater.* **2018**, *8*, 1703288.
[17] a) X. Ou, L. Cao, X. Liang, F. Zheng, H.-S. Zheng, X. Yang, J.-H. Wang, C. Yang, M. Liu, *ACS Nano* **2019**, *13*, 3666-3676; b) L. Cao, X. Gao, B. Zhang, X. Ou, J. Zhang, W.-B. Luo, *ACS Nano* **2020**, *14*, 3610-3620.
[18] S. Yu, S. O. Kim, H. S. Kim, W. Choi, *Int. J. Energy Res.* **2019**, *43*, 7646-7654.
[19] J. Sangster, A. Pelton, *J. Phase Equilib.* **1993**, *14*, 510-514.
[20] M. Mayo, A. J. Morris, *Chem. Mater.* **2017**, *29*, 5787-5795.
[21] I. Sultana, M. M. Rahman, Y. Chen, A. M. Glushenkov, *Adv. Funct. Mater.* **2018**, *28*, 1703857.
[22] V. Gabaudan, R. Berthelot, L. Stievano, L. Monconduit, *J. Phys. Chem. C* **2018**, *122*, 18266-18273.
[23] a) Y. Gao, W. Tian, C. Huo, K. Zhang, S. Guo, S. Zhang, X. Song, L. Jiang, K. Huo, H. Zeng, *J. Mater. Chem. A* **2019**, *7*, 3238-3243; b) W. Tian, S. Zhang, C. Huo, D. Zhu, Q. Li, L. Wang, X. Ren, L. Xie, S. Guo, P. K. Chu, H. Zeng, K. Huo, *ACS Nano* **2018**, *12*, 1887-1893.
[24] M. R. Palacin, *Chem. Soc. Rev.* **2009**, *38*, 2565-2575.
[25] H. Wang, D. Zhai, F. Kang, *Energy Environ. Sci.* **2020**.
[26] Y. Li, Li, Y., Pei, A., Yan, K., Sun, Y., Wu, C.L., Joubert, L.M., Chin, R., Koh, A.L., Yu, Y. and Perrino, J., , *Sicence* **2017**, *58(6362)*, 506-510.
[27] H. Hertz, *J. Reine Angew. Math.* **1881**, *92*, 156-171.
[28] a) K. L. Johnson, K. L. Johnson, *Contact mechanics*, Cambridge university press, **1987**; b) Y. Gao, S.-Q. Shi, T.-Y. Zhang, *Nanoscale* **2017**, *9*, 6033-6040.
[29] H. Bryngelsson, M. Stjerndahl, T. Gustafsson, K. Edström, *J. Power Sources* **2007**, *174*, 970-975.
[30] S. Chattopadhyay, A. L. Lipson, H. J. Karmel, J. D. Emery, T. T. Fister, P. A. Fenter, M. C. Hersam, M. J. Bedzyk, *Chem. Mater.* **2012**, *24*, 3038-3043.
[31] a) D. Bar-Tow, E. Peled, L. Burstein, *J. Electrochem. Soc.* **1999**, *146*, 824; b) A. Andersson, K. Edström, *J. Electrochem. Soc.* **2001**, *148*, A1100.
[32] a) D. Aurbach, E. Pollak, R. Elazari, G. Salitra, C. S. Kelley, J. Affinito, *J. Electrochem. Soc.* **2009**, *156*, A694; b) L. Lodovico, A. Varzi, S. Passerini, *J. Electrochem. Soc.* **2017**, *164*, A1812.
[33] D. Aurbach, *J. Power Sources* **2000**, *89*, 206-218.
[34] L. Deng, Y. Zhang, R. Wang, M. Feng, X. Niu, L. Tan, Y. Zhu, *ACS Appl. Mater. Interfaces* **2019**, *11*, 22449-22456.
[35] Q. Zhang, J. Pan, P. Lu, Z. Liu, M. W. Verbrugge, B. W. Sheldon, Y.-T. Cheng, Y. Qi, X. Xiao, *Nano Lett.* **2016**, *16*, 2011-2016.
[36] L. Xue, Y. Li, H. Gao, W. Zhou, X. Lü, W. Kaveevivitchai, A. Manthiram, J. B. Goodenough, *J. Am. Chem. Soc.* **2017**, *139*, 2164-2167.